

# The effect of supercapacitors in a tidal current conversion system using a torque pulsation mitigation strategy



# The Effect of Supercapacitors in a Tidal Current Conversion System using a Torque Pulsation Mitigation Strategy

Marios Charilaos Sousounis, corresponding author: M.Sousounis@ed.ac.uk

Jonathan K.H. Shek, and Brian G. Sellar

*School of Engineering, Institute for Energy Systems, The University of Edinburgh, Faraday Building, King's Buildings, Colin Maclaurin Road, Edinburgh EH9 3DW, UK.*

**Abstract**

The research presented in this paper investigates the effect of connecting supercapacitors at the DC link of a hypothetical 1.5MW three-bladed variable-pitch horizontal-axis tidal current turbine that uses a torque pulsation mitigation strategy. Torque pulsations are classified into fatigue torque and ultimate or peak torque. Both can lead to premature components failure or system overdesign and costly maintenance. Research has suggested that torque pulsations can be mitigated by using a novel control strategy with which pulsations created by the unsteady tidal current flow are reduced by changing the generator speed. Increasing the variation of the generator speed increases the variation of the electrical power output of the generator. The electrical power output of the generator is injected to the grid through back-to-back AC to DC, DC to AC converters. The increased variation of the electrical power output of the generator causes DC link voltage spikes, increases the stress of electrical components and affects the compliance of the tidal current conversion system for grid connection. In order to tackle these problems a supercapacitor module is proposed to be connected at the DC link. The supercapacitor is able to absorb the fast short-term variations of the electrical power and keep the DC link voltage within limits. The potential benefits of using supercapacitors for connection in weaker grids and in tidal current arrays are also studied. Results show that DC link voltage and grid side harmonics are positively affected from the installation of a supercapacitor at the DC link.

**Keywords**: Tidal current conversion system; Energy storage; Supercapacitor; Torque pulsation; Generator control; Voltage control;

## 1. Introduction

Tidal current energy is clean, renewable and predictable. Tidal currents are created by the changing gravitational pull of the Moon and the Sun on the Earth's oceans. Depending on the location on

Earth, tides occur approximately every 24 hours and 50 minutes (Diurnal), every 12 hours and 25 minutes (Semi-Diurnal) or can be mixed. The predictability of tidal current energy is a major advantage for integrating power to the grid compared to the intermittent wind energy or the weather dependant solar energy. However, short-term power fluctuations in a tidal current conversion system (TCCS) occur due to turbulence and swell waves. These short-term power fluctuations can be regulated using electrical energy storage (EES) [1] to increase grid stability (voltage and frequency) and keep harmonics injected to the grid as low as possible. This is important because tidal current resource is usually exploitable close to rural coastal areas where the electricity network is weak. In this paper, research will focus on the effect of installing supercapacitors (SCs) in a TCCS in order to improve grid side harmonics and keep DC link voltage within allowable limits.

The technically available tidal current energy resource in the United Kingdom can supply up to 11.3% of the UK electricity demand based on 2016 statistics [2,3].The tidal currents move slowly relative to typical wind currents but possess very high energy density. As a result of the high energy density, TCCSs are subjected to large forces. Despite the large forces exerted on the tidal current turbines, TCCSs are expected to extract the maximum from the available energy and operate reliably under the harsh underwater conditions. In this paper, the research presents that by controlling the generator speed with larger variations it is possible to reduce extreme and fatigue torque loadings on the tidal current turbines. Combining this with the SCs at the TCCS it is possible to achieve both reduced torque loadings and higher quality electrical power at the grid side.

## 1.1 Research on energy storage in tidal current systems

ESS usage in tidal current systems depends mainly on the duration of the effect that the storage will be used. In [4] authors present an overview of current developments in EES technologies and their potential applications and effects on power system operation. Similar research is presented in [1] where the different storage techniques are separated into four categories with a performance index.

- Low power applications in isolated areas (Lead-acid batteries, flow batteries and lithium-ion batteries).

- Medium power off-grid systems (Lead-acid batteries, flow batteries, nickel-cadmium batteries and lithium-ion batteries).
- Network connection applications (SCs, compressed air, lithium-ion batteries).
- Power quality control applications (SCs, flywheels and compressed air).

A more specific review on EES in tidal systems is presented in [5]. Researchers in [5] categorise the tidal fluctuations and test different EES in order to smooth variability of electrical power injected to the grid. The EES options discussed include lead-acid batteries, nickel-based batteries, lithium-ion batteries, sodium-sulphur batteries, flow batteries, flywheel technologies and SC technologies. They conclude that for long-term power smoothing in tidal current systems nickel-based batteries are a good solution. Regarding compensating power fluctuations for the short-term flywheel and SCs are the optimum candidates. In [6] researchers use a SC connected at the DC link in order to compensate for the swell effect. They show that with the use of a SC and a DC/DC converter the short term variations of the grid side current can be minimised. Other research in ESS in tidal systems has focused on the use of compressed air energy storage (CAES) for island systems [7,8] and flow batteries for power management [9] as well as dynamic stability using flywheel energy storage in an offshore wind and tidal system [10].

Apart from the research that directly focuses on tidal current systems, significant research on energy storage is being carried out that can be easily integrated in a TCCS. The CAES is a technology with high economic feasibility, flexible power ratings and proven technology. Research has focused on the integration of CAES in renewable energy systems [11,12] and in the development of underwater CAES [12,13] which can have increased energy storage capabilities. Research on underwater storage is gaining attention and can be easily integrated in a TCCS which is also underwater. Several other concepts for underwater storage also appear with buoyant energy storage to be integrated to large renewable energy generation systems [14,15] for power balancing and offshore pump storage to store large amount of energy at the sea.

## 1.2 Research on forces and moments in tidal current devices

Significant research has been carried out in order to understand loadings and bending moments during normal and extreme conditions. Some studies have focused on the nature of the tidal current

flow due to phenomena such as shear flow, turbulence and waves which generate unstable forces and moments on the device [16–20]. Researchers have focused on minimising the unbalanced forces and moments as well as trying to avoid extreme cases.

The most common way to limit peak loads is to limit the power output of the turbine by using pitch control, stall regulation or over-speeding. In [21] authors analysed the performance of pitch and stall regulated turbines. They concluded that pitching to feather the blade regulated power output and generated lower bending moments compared to stalling the blade. Authors in [22] also compare pitching the blades of a marine hydrokinetic turbine to passively stalling the blades or designing a blade to have lower loads. They concluded that blades can be designed to have reduced bending moments but will also extract less power from the tidal currents. Over-speeding the turbine is another method to limit power input to the turbine. In [23] researchers analyse thoroughly the over-speeding method in a tidal current turbine and modify blade design accordingly. Finally, a novel method to reduce torque variations and peak torque on the turbine shaft was presented in [24]. This method uses the generator side converter to vary the generator speed in order to achieve a smoother torque input to the turbine. The torque pulsation mitigation strategy with which the system in this paper will be tested is based on the one presented in [24]. The need to vary the generator speed to reduce the mechanical torque variations on the turbine generates variations on the electrical side. These become more visible at the DC link and electrical power generated. It is suggested that these fast short-term variations of electrical power can be smoothed using a SC at the DC link.

## 1.3 Paper aim and structure

The aim of this paper is to present a full resource-to-grid dynamic model of a single tidal current turbine with a supercapacitor module (SCM) connected at the DC link. The tidal system model will be controlled using the novel strategy presented in [24] and the benefits of using the SCM at the DC link will be investigated. In Section 2 the modelling of the resource-to-grid system is presented including the tidal current resource input, tidal current turbine design, the different control strategies implemented and the SCM with the associated control strategy and design. In Section 3 results from the simulations of the model are presented showing and comparing the differences between a tidal system that uses the SCM and one without. Results are separated

depending on the controller aim to mitigating sudden flow changes only or reducing fatigue torque. In addition, the use of a SCM in a tidal array concept connected to weaker, more isolated grid networks is studied. Finally, the discussion shows the potential use of this concept in a wider scope and conclusions are drawn regarding the use of the SCM at the DC link.

## 2. Methodology

The block diagram of the tidal current system developed in MATLAB/Simulink is depicted in Figure 1.

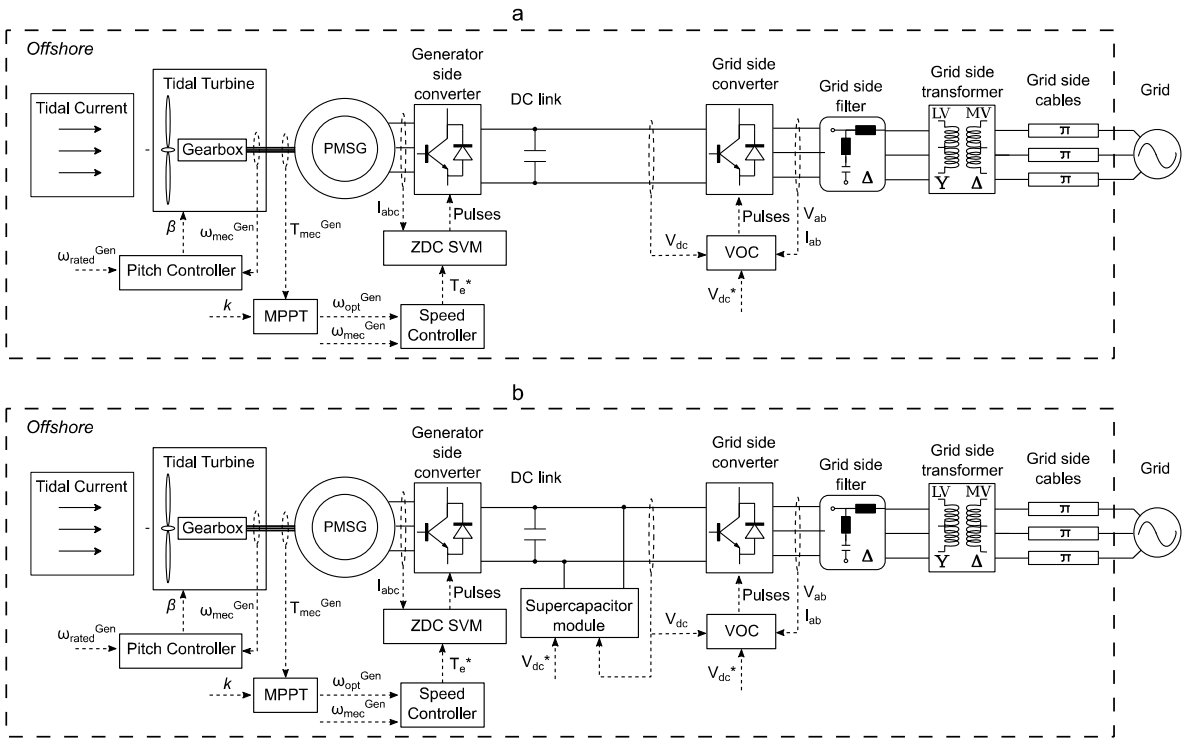


**Figure 1. Block diagram of the resource-to-grid model developed in MATLAB/Simulink. a. Tidal current conversion system without a Supercapacitor module. b. Tidal current conversion system with the Supercapacitor module connected at the DC link.**

Each part of the tidal current conversion system shown in Figure 1 will be explained in the sections below. Section 2.1 discusses the tidal current input, section 2.2 the tidal turbine design, modelling and the pitch controller, section 2.3 briefly gives the permanent magnet synchronous generator (PMSG) parameters and explains the zero d-axis current controller with space vector modulation (ZDC SVM) and section 2.4 discusses the maximum power point tracking (MPPT) process and

how the PMSG can track the $\omega_{opt}{}^{Gen}$ using the speed controller. Moreover, in section 2.5 details regarding the torque pulsation mitigation methods are given, in section 2.6 the Supercapacitor module and its control are explained and finally in section 2.7 the voltage oriented control (VOC) for the grid side converter is analysed.

## 2.1 The tidal current

The tidal current input to the tidal turbine model comprises timeseries of flow velocities acquired during field measurement campaigns conducted by the University of Edinburgh at the European Marine Energy Centre (EMEC) tidal test site in Orkney, UK during the Reliable Data Acquisition Platform for Tidal project (ReDAPT) between 2011 and 2015. Environmental data acquired up to October 2014 is publicly available at the UKERC Energy Data Centre [25] and at [26]. Depth profiles of velocity measurements were provided by seabed mounted divergent beam acoustic Doppler profilers (D-ADP) deployed at depths between 43 m and 46 m to the north-west and south-east of the Alstom DEEP-Gen IV tidal turbine (on the flood and ebb tides respectively). Multiple D-ADPs were installed at distances varying between approximately 40 m and 100 m from the turbine rotor plane as described in more detail in [27]. In addition to industry-standard D-ADP deployments, multiple single-beam acoustic Doppler profilers (SB-ADP) were installed on the TEC at top-rearward, rear and nose locations. Unlike divergent beam ADPs, single-beam ADPs measure velocities directly along an axis of interest (in this case orientated with respect to the flow in stream-wise, vertical and transverse directions) [27]. An SB-ADP installed on the TEC rotating hub and orientated in a stream-wise direction provides near-field flow information directly from mid-depth (TEC hub-height). Provided velocity profiles feature cell sizes of 0.4 m to 0.5 m at sample rates of 2 Hz or 4 Hz depending on configuration. Periods of high wave activity were identified by turbine-installed single-beam ADP (SB-ADP) orientated in the vertical direction. Field measurement techniques and subsequent data processing are discussed more fully in [28,29].

Figure 2 depicts two cases of tidal current speeds used as input to the model as measured by the TEC hub mounted single-beam ADP. Figure 2a shows timeseries tidal current velocity data with mean velocity of 2.3 m/s and a sea-state, measured directly above the TEC, exhibiting significant wave heights of less than 0.3 m. Figure 2b shows timeseries tidal current velocity data with mean

velocity of 2.0 m/s and a sea-state with large waves, featuring significant wave heights of 1.9 m and peak periods of 9 seconds. Flow turbulence is visible at multiple scales and appears to include large, low-frequency gusts. Sudden flow changes can be seen in Figure 2a around 7365s and 7410s. Similarly in Figure 2b sudden flow changes appear around 12230s and 12275s.

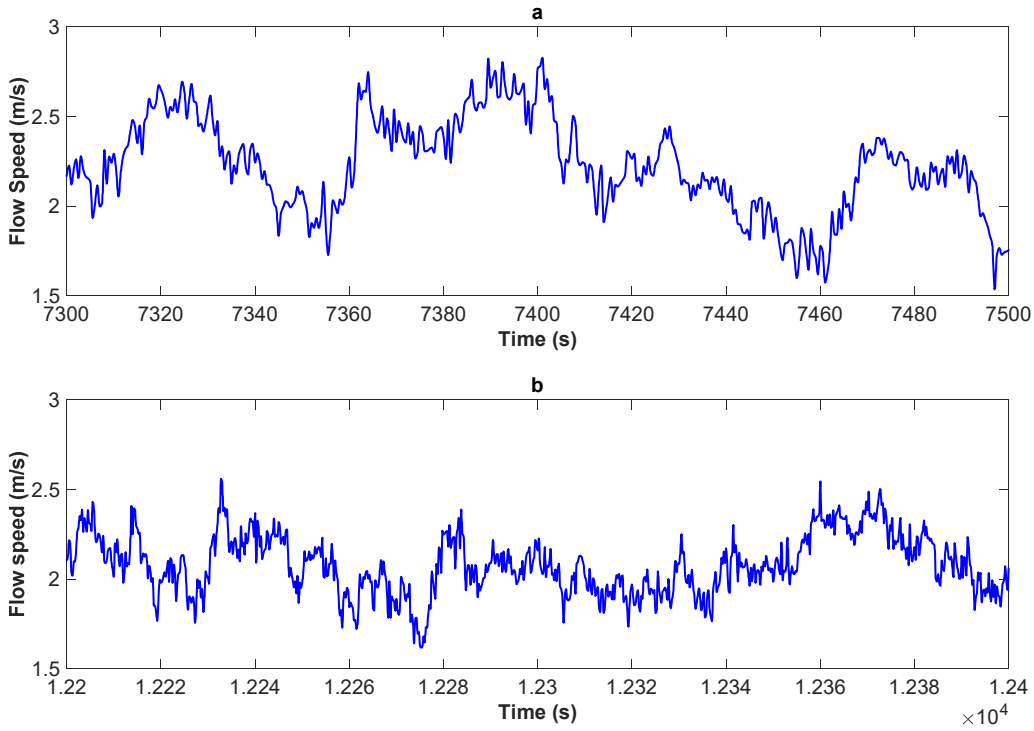


**Figure 2. Timeseries data of tidal current velocities in the stream-wise direction acquired from TEC hub-height during the ReDAPT project. a. Low wave condition b. Large wave condition**

The tidal current velocity measurements presented in Figure 2 are acquired in real-time from a region approximately 13 m upstream of the TEC rotor plane. Knowledge of the ambient flow velocity, acquired at an equivalent of several seconds before it reaches the rotor plane, is a required input control signal in order to mitigate pulsations using the generator side controller. In addition, high resolution velocimetry is important to identify realistic changes in the tidal current speed which affects the operation of the torque pulsation mitigation strategy and the response time of the SCM. Finally, the real-time availability of measurements is crucial for the operation of the system.

The power input to the tidal current turbine is related to the data of Figure 2 based on (1).

$$P_{tide} = \frac{1}{2} \cdot \rho_{water} \cdot A \cdot V^3 \quad \textbf{(1)}$$

Where $\rho_{water}$ is the sea water density in kg/m$^3$, $A$ is the sweep area in m$^2$ and $V$ is the fluid speed in m/s. Figure 3 depicts the power of the tidal current velocity used as input to the tidal current turbine model. Based on the results of Figure 3 it can be observed that significant power variations can occur during a tidal cycle. For example, at 7360s the power of the tide varies from approximately 2MW to 3.5MW in approximately 5s and at around 7400s the power of the tide drops from 3.9MW to 2MW in approximately 10s. These sudden power variations can adversely affect the voltage and frequency stability of the grid, especially when a weak grid is considered.

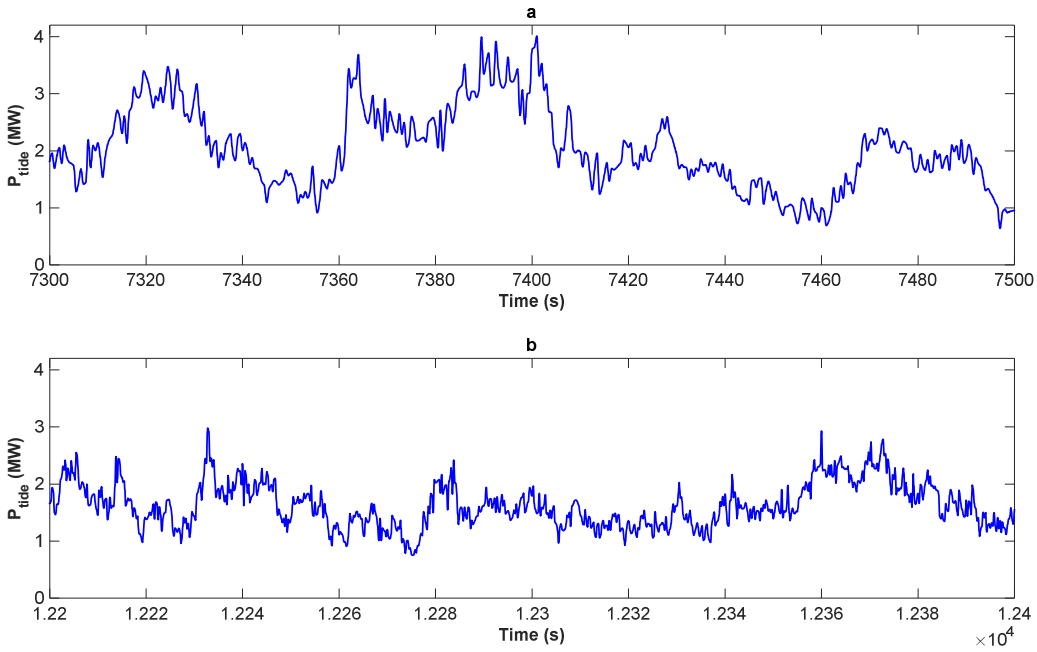


**Figure 3. Timeseries data of tidal current power calculated using (1). a. Low wave condition b. Large wave condition.**

## 2.2 The tidal current turbine

The tidal turbine model converts the power input from the tidal current to mechanical power for the generator rotor. Equation (2) describes the mechanical power of the turbine from the tidal current velocity. The output of the tidal current turbine is mechanical torque, $T_{\text{mec}}$, which is used as input to the generator after the gearbox ratio is considered.

$$P_{turbine} = \frac{1}{2} \cdot \rho_{water} \cdot A \cdot C_p(\lambda, \beta) \cdot V^3 \quad \textbf{(2)}$$

$$T_{mec} = \frac{P_{turbine}}{\omega_r} \quad \textbf{(3)}$$

Where $\omega_r$ is the rotational speed of the tidal current turbine in rad/s, $\rho_{water}$ is the sea water density in kg/m$^3$, $A$ is the sweep area in m$^2$, $V$ is the fluid speed in m/s and $C_p(\lambda,\beta)$ is the power coefficient of the blades which is a function of the tip speed ratio, $\lambda$, and blade pitch angle, $\beta$, in degrees. The tips speed ratio is given in (4) where $R$ is the turbine rotor radius.

$$\lambda = \frac{\omega_r \cdot R}{V} \quad \textbf{(4)}$$

The tidal current turbine used in this paper is a hypothetical three-bladed horizontal-axis 1.5MW turbine. The numerical tool of Harp_Opt [30] was used which combines blade element momentum theory with a genetic algorithm to generate a structurally optimised blade design. From the outputs of Harp_Opt the $C_p$ curve of the turbine as well as turbine inertia and gearbox ratio were calculated. The tidal current turbine specifications used are given in Table 1 and the $C_p(\lambda)$ curve for different pitch angles, $\beta$, in Figure 4.

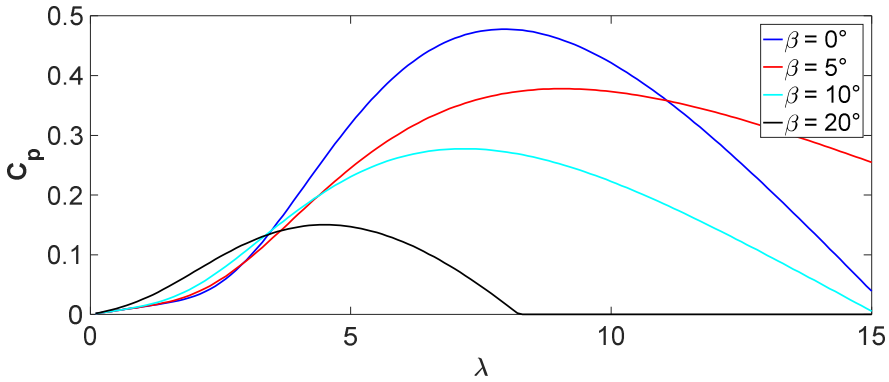


**Figure 4. Hydrodynamic coefficient of the tidal current turbine modelled for different pitch angles.**

**Table 1. Tidal turbine parameters.**

| Parameter | Value | Units |
|---|---|---|
| Rated power | 1.5 | MW |
| Rotor diameter | 23 | m |
| Hub diameter | 2 | m |

| | | |
|---|---|---|
| Maximum $C_p$ | 0.4777 | - |
| Optimum $\lambda$ | 7.95 | - |
| Base tidal flow speed | 2.5 | m/s |
| Inertia | 178540 | kg.m$^2$ |
| Gearbox ratio | 66.6667 | - |

The power coefficient, $C_p(\lambda,\beta)$, was approximated using an analytic function described in [31]. This analytic function is given in (5) and (6) and the chosen values for the tidal turbine are shown in Table 2.

$$C_p(\lambda,\beta) = c_1\left(\frac{c_2}{\lambda_i} - c_3 \times \beta - c_4\right)e^{-\frac{c_5}{\lambda_i}} + c_6 \times \lambda \quad \textbf{(5)}$$

$$\frac{1}{\lambda_i} = \frac{1}{\lambda + 0.08 \times \beta} - \frac{0.035}{\beta^3 + 1} \quad \textbf{(6)}$$

**Table 2 Coefficients chosen for the approximation of the $C_p(\lambda,\beta)$ curve of the tidal turbine.**

| $c_1$ | $c_2$ | $c_3$ | $c_4$ | $c_5$ | $c_6$ |
|---|---|---|---|---|---|
| 0.3489 | 100 | 0.4 | 3.932 | 17.25 | 0.01292 |

### 2.2.1 The pitch control

Power limitation in high tidal current speeds is achieved by using pitch angle control. This corresponds to changing the pitch value, $\beta$, such that the leading edge of the blade is moved into the flow increasing the angle of attack and thus inducing a blade feathering effect. When tidal current speed is below or at the rated value of the turbine, pitch angle, $\beta$, is kept constant. For reference this is chosen to be the 0 degrees. The control structure of the pitching system developed is shown in Figure 5. The measured generator rotational speed $\omega_{mec}{}^{Gen}$ is compared with the desirable rated generator rotational speed, $\omega_{rated}{}^{Gen}$, and the error is used as input to a Proportional-Integral (PI) controller. The PI controller output is the desirable pitch angle input, $\beta_{ref}$, which is constrained due to the dynamics of the actuator, maximum speed of the blade pitching system and maximum blade pitch angle. After the constraints have been considered, the actual blade pitch angle, $\beta$, is used as input to the tidal current turbine. The pitching mechanism limits the generator power output to rated by reducing $C_p$ in (2) and so reducing the mechanical power captured.

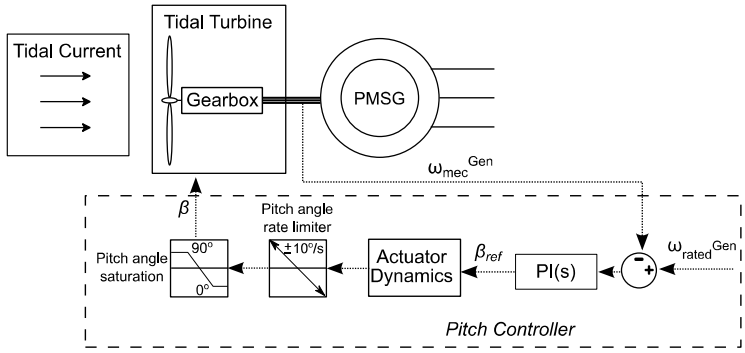


**Figure 5. Block diagram of the pitch controller implemented in MATLAB/Simulink.**

## 2.3 The generator

The generator modelled is a hypothetical non-salient pole PMSG with the specifications of Table 3.

**Table 3. PMSG parameters.**

| Parameter | Value | Units |
|---|---|---|
| Rated power | 1.5 | MW |
| Line voltage | 690 | $V_{rms}$ |
| Stator phase resistance | 0.004 | Ω |
| Stator phase inductance | 0.001 | H |
| Flux induced by magnets, $\lambda_r$ | 1.7933 | Wb |
| Pole pairs, $p$ | 3 | - |
| Inertia | 45 | $kg.m^2$ |
| Viscous damping | 2.3 | N.m.s |
| Synchronous speed | 104.6 | rad/s |

### 2.3.1 The generator controller

The generator controller is described in [32] and is based on zero d-axis current control with space vector modulation (ZDC SVM). The ZDC SVM control method for non-salient pole PMSG is based on the linear relationship between the stator current magnitude, $i_s$, and the electromagnetic torque, $T_e$ when the d-axis stator current of the generator is kept zero and the flux, $\lambda_r$, is kept constant. The block diagram of the ZDC SVM controller can be seen in Figure 6.

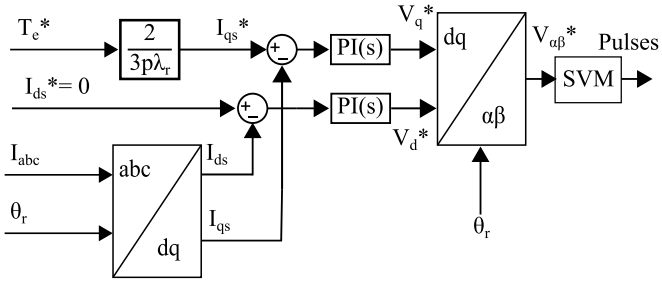


**Figure 6. Block diagram of the ZDC SVM generator controller** [32]**.**

## 2.4 Maximum power point tracking

Maximum power point tracking (MPPT) has one major aim: to control the tidal turbine's Tip Speed Ratio $\lambda$ in order to achieve the highest possible hydrodynamic coefficient $C_p$. MPPT is responsible for the efficient operation of the tidal current system at tidal current speeds below 2.5m/s, which is the base tidal flow speed. In order to achieve the efficient operation, first the operating points where maximum $C_p$ is achieved must be identified. These operating point form the maximum power point curve. After creating the maximum power point curve the speed and torque of the generator have to be controlled in order to achieve these optimised operating points. This is achieved by the speed controller.

### 2.4.1 Maximum power point curve

The maximum power point curve identifies all the operating points with maximum $C_p$. The maximum power point curve modelled in this paper is based on equation (8) where $k$ is a constant equal to 1.3193. The generator mechanical torque, $T_{mec}^{Gen}$ can be either available as a direct measurement from a torque transducer or can be estimated using equation (7).

$$T_{mec}^{Gen} = k \cdot {\omega_{opt}^{Gen}}^2 \Leftrightarrow \omega_{opt}^{Gen} = \sqrt{\frac{T_{mec}^{Gen}}{k}} \quad \textbf{(8)}$$

### 2.4.2 Speed controller

The speed controller is responsible for comparing the optimum generator speed, ${\omega_{opt}}^{Gen}$, acquired by equation (8) and actual generator speed, ${\omega_{mec}}^{Gen}$, which is measured, in order to produce a reference signal for the electromagnetic torque of the generator. The reference signal of the

electromagnetic torque, $T_e$*, is used as input to the generator controller ZDC SVM shown in Figure 6. The block diagram of the speed controller is shown in Figure 7. More details can be found in [24].

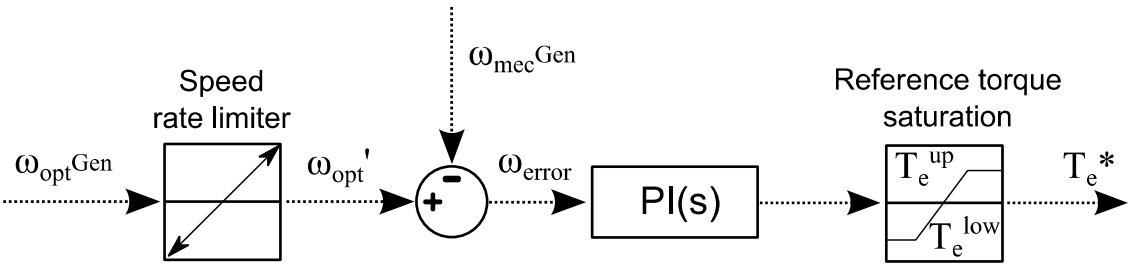


**Figure 7. Speed controller block diagram as modelled in MATLAB/Simulink.**

## 2.5 Torque pulsation mitigation strategy

The torque pulsation mitigation strategy used in this paper is based on the methodology presented in [24]. Pulsations are classified into:

1) Ultimate torque
2) Fatigue torque.

In [24] authors present results for both methods by modifying the coefficient *k* and therefore forcing the generator to follow a different reference speed, with the aim to reduce the ultimate torque value or the torque variations. Figure 8a presents the block diagram of the ultimate torque mitigation (UTM) strategy and Figure 8b the block diagram of the fatigue torque mitigation (FTM) strategy.

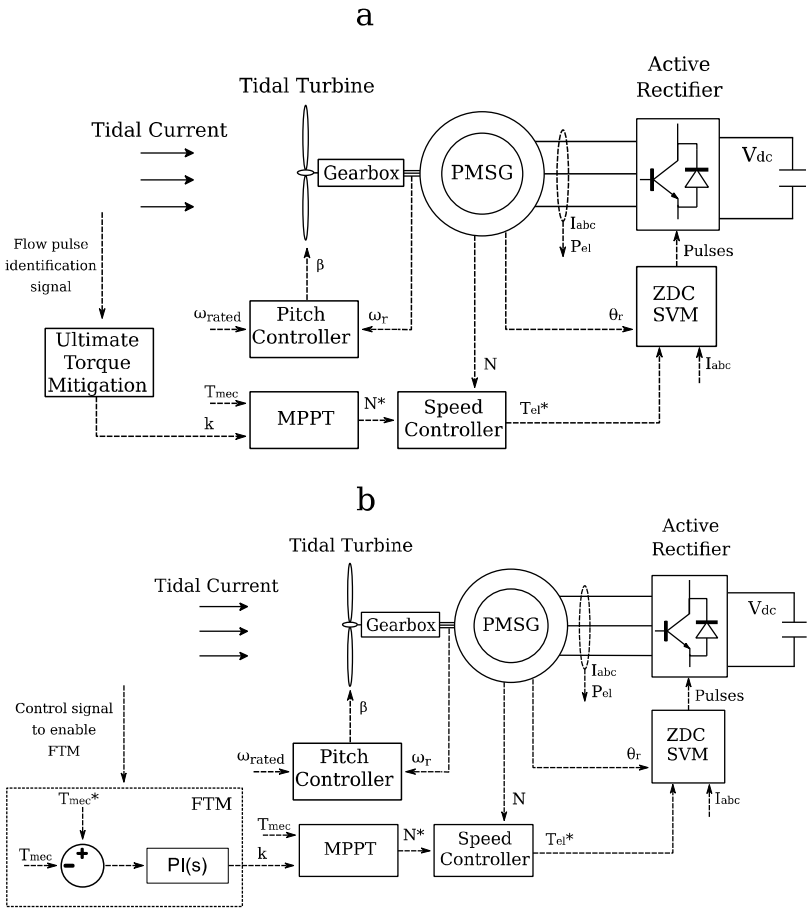


**Figure 8. Block diagrams of the torque pulsation mitigation strategies for a. UTM b. FTM. Presented in [24].**

The UTM control strategy's aim is to reduce the peak value of a torque pulsation. In order to achieve that the MPPT coefficient *k* discussed in Section 2.4.1 is reduced to a lower value so that $C_p$ is no longer maximum. By doing that the tidal current turbine will absorb less power from the tidal currents reducing the magnitude of the mechanical torque at the shaft. However, and as it can be seen from Figure 2 tidal current velocities can change suddenly making it impossible for the turbine to change its speed after the sudden flow increase has reached the turbine. For that reason it is essential to identify the incoming flow pulse in advance using a flow velocity sensor such as seabed or turbine mounted ADPs as discussed in Section 2.1. Velocimetry and the process to identify sudden increases in the tidal current speed are out of the scope of this paper but the concept relies on analysing data from the ADP online to identify a sudden tidal current velocity increase. By identifying a sudden velocity increase the appropriate *flow pulse identification signal* (ON or

OFF) can be provided to enable the UTM control strategy. Therefore it is evident that the UTM method only operates for a specific amount of time depending on the time the sudden tidal current velocity increase lasts. This can vary between 5 and 10 seconds based on the actually measured data presented in Section 2.1. The FTM control strategy, which is presented in Figure 8b, aims to reduce both the peaks and troughs of the mechanical torque input $T_{mec}$. This is achieved by modifying the MPPT coefficient $k$ to lower and higher values depending on the difference between $T_{mec}$ and $T_{mec}$*. When $T_{mec} > T_{mec}$* the generator over-speeds to reduce $C_p$ while when $T_{mec} < T_{mec}$* the generator under-speeds and puts the tidal current system in a state of regenerative braking. This operation is constrained so that the system remains stable. The FTM method is designed so that it can replace the MPPT strategies that are currently used for normal operation and increase the lifetime of components due to lower torque loading. This means that the FTM method can operate during the whole tidal cycle. The UTM and FTM methods can also be combined to operate is the same system, however this is not demonstrated in this paper and results are presented individually in Section 3.

The torque pulsation mitigation strategies presented in Figure 8 require to change the optimum generator speed in order to change the mechanical torque input. This leads to increased variations of the generator speed which affects the quality of the power generated. The quality of power is assessed based on the planning levels for harmonic voltage distortion from the Engineering Recommendation G5/4-1[33] which are in line with the international standard IEC 61000-3-6. In this paper the use of SCs is studied in order to increase the power quality of the power generated from these control methods.

## 2.6 The supercapacitor module design and control

The supercapacitor module (SCM) is connected to the DC link using a bi-directional DC/DC Cuk converter [34]. The bidirectional DC/DC Ćuk converter can be implemented by cascading the boost converter and the buck converter similarly to a buck-boost converter. The Ćuk converter however, is composed from an input inductor *L1*, an energy transfer capacitor *C1*, a filter inductor *L2*, a filter capacitor *C2* and two switching devices as shown in Figure 9a. Therefore the Ćuk converter requires two capacitors and two inductors compared to the one capacitor and one inductor with which the buck-boost converter is composed. The additional components offer a

number of advantages which makes the Ćuk converter an interesting alternative for their use with supercapacitors. First of all the Ćuk converter does not require additional *L-C* filters like a buck-boost converter as its topology offers non-pulsating input and output currents. In addition, the DC gain of the Ćuk converter is higher compared to a buck-boost converter. This makes it possible to connect less supercapacitors to form the SCM and step up the voltage to match the DC link voltage at 1450V. Finally, for control purposes, the Ćuk converter has a more stable open-loop transfer function compared to the buck-boost converter [34]. The utilisation of a bidirectional DC/DC Ćuk converter with a SC system in a wave energy array is described in [35]. The control system of the bidirectional DC/DC Ćuk converter implemented in this study is based on the voltage-mode control and is presented in Figure 9b. At this mode the controller tries to keep the voltage at a reference value. The error between the reference voltage and actual voltage is used as input to a PID controller in order to construct a control voltage signal. The voltage control signal is then utilised to generate high frequency PWM signals at 10 kHz for the switching devices *S1* and *S2*. Despite the fact that, as it will be presented in Section 2.7, the DC link voltage is controlled through the grid side converter, the voltage-mode control of the bidirectional DC/DC Ćuk converter is preferred because:

- The input and output variations are wide and, as is shown in Section 3, increase further due to the operation of the torque pulsation mitigation control strategy.
- The operation of the system is kept stable even at reduced input. Low input results will not be shown in this study but the tidal current conversion system presented in this paper was developed as tool which can predict the operation of a resource-to-grid system for the complete tidal cycle.
- Because of the high power application and the fluctuating current input, current-mode control would require large time delays for filtering which could lead to a slow response system.

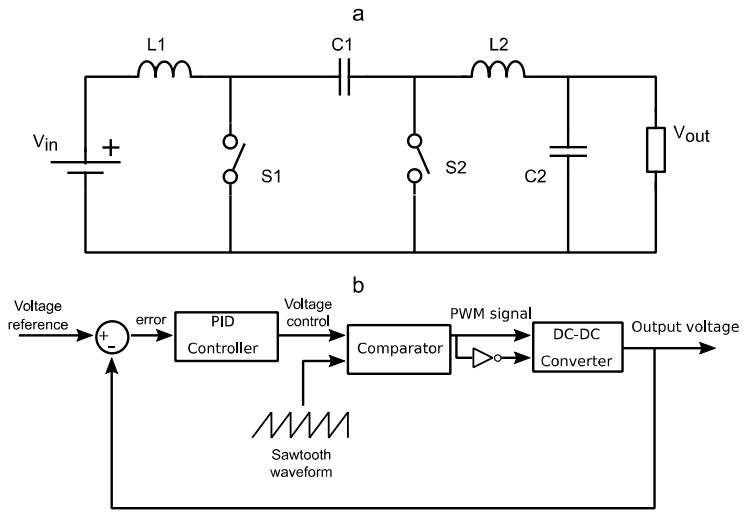


**Figure 9.a. Schematic diagram of the bi-directional DC/DC converter. b. Voltage-mode control of the bi-directional Ćuk converter.**

The SC voltage is chosen to be 750V and this is possible by adding six in series BMOD0063 P125 B08 SC modules from Maxwell Technologies [36]. The SC voltage requires to be high enough in order to avoid saturating the controller of the Ćuk converter. From the total energy stored in the SCM only 20% of that is useable in this application because a ±10% of voltage variation is allowed. The parameters of the SCM are presented in Table 4.

**Table 4. SCM parameters.**

| Symbol | Quantity | Value |
|---|---|---|
| $V_{dc}$ | DC link voltage | 1450 $V$ |
| $V_{cap}$ | SC voltage | 125 $V$ |
| $C_{cap}$ | SC capacitance | 63 F |
| $ESR_{cap}$ | SC ESR | 18 mΩ |
| $E_{cap}$ | SC stored energy | 152 $Wh$ |
| $N_{cap}$ | Number of SCs in series | 6 |

## 2.7 The grid side modelling and control

The power generated by the TCCS is delivered to the grid through a voltage-source converter (VSC). The grid-tied inverter is connected to the grid through a number of components; a line

reactor to reduce line current distortion, a filter that reduces harmonics and a step-up transformer from 690V to 11kV (Figure 10).

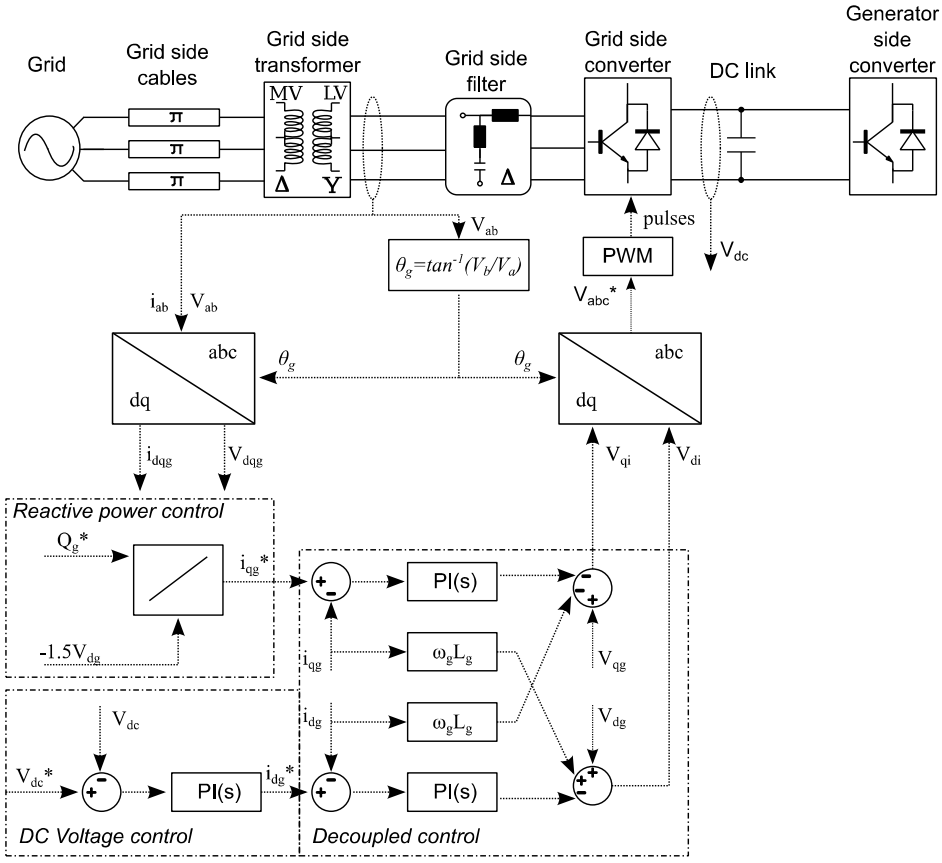


**Figure 10. VOC controller as implemented in MATLAB/Simulink.**

The inverter is controlled by a PWM scheme called voltage oriented control (VOC) with decoupled controllers which ensures a constant DC link voltage, constant frequency output of 50Hz on the AC side and control over the amount of reactive power flowing based on grid requirements. The switching frequency of the PWM scheme is at 2.5 kHz. The VOC scheme is based on (9):

$$\begin{cases} \boldsymbol{V_{di}(t) = -\left[K_P^I\left(i_{dg}^* - i_{dg}\right) + K_I^I \int \left(i_{dg}^* - i_{dg}\right)dt\right] + \omega_g L_g i_{qg} + V_{dg}} \\ \boldsymbol{V_{qi}(t) = -\left[K_P^I\left(i_{qg}^* - i_{qg}\right) + K_I^I \int \left(i_{qg}^* - i_{qg}\right)dt\right] - \omega_g L_g i_{dg} + V_{qg}} \end{cases} \quad \textbf{(9)}$$

The tuning process for the VOC control loops was based on [37] in which authors use the symmetric optimum criterion to tune the ac current and the dc voltage controllers. At first the

decoupled inner current controllers were tuned. The proportional gain was chosen to be $K_p^I = 0.3$ and the integral gain $K_i^I = 30$. The stability margins of the inner current controllers (61.7° phase margin and 22.5dB gain margin) are adequate to ensure the stable operation of the control system under uncertainties. The bandwidth of the current controllers is $f_c^I = 244$Hz which is more than 10 times smaller than the switching frequency of the PWM signal which ensures minimal interference from the switching frequency harmonics. In addition, the step characteristics of the current controllers demonstrate adequate response with maximum overshoot of 1.13 and settling time of 0.05s. Having tuned the inner current control loops the outer DC link voltage loop controller is tuned in order to have good stability margins and bandwidth smaller than the bandwidth of the inner current control loops. Based on these requirements the DC voltage controller gains are chosen as $K_p^V = 1.3888$ and $K_i^V = 400$. The stability margins for the DC voltage controller are 60° phase and 9dB gain margin and the bandwidth is $f_c^V = 23$Hz.

# 3. Results

The MATLAB/Simulink model of Figure 1 was simulated under different conditions in order to determine the benefits of using the SCM at the DC link. The first set of simulations explore the effects of sudden flow changes and the usage of UTM to reduce peak torque. The second set of simulations explore the fatigue torque variations and the operation of FTM to reduce torque variations. Finally, the use of the SCM is assessed when used in a tidal array concept connected at stronger or weaker networks.

## 3.1 Sudden flow changes

The MATLAB/Simulink model of Figure 1 was simulated for 100 seconds under three different control strategies using the tidal current speed input presented in Figure 2.

- The first is maximum power point operation (MPPO) which was described in Section 2.4 without a SCM at the DC link.
- The second is UTM which was described in Section 2.5 and Figure 8a without a SCM at the DC link.
- The third is the UTM method when the SCM is installed at the DC link.

It has to be noted that for this set of simulations the TCCS is assumed to be connected to a strong grid with 50MVA 3-phase fault level. Figure 11 shows results from the operation of the TCCS under each control strategy.

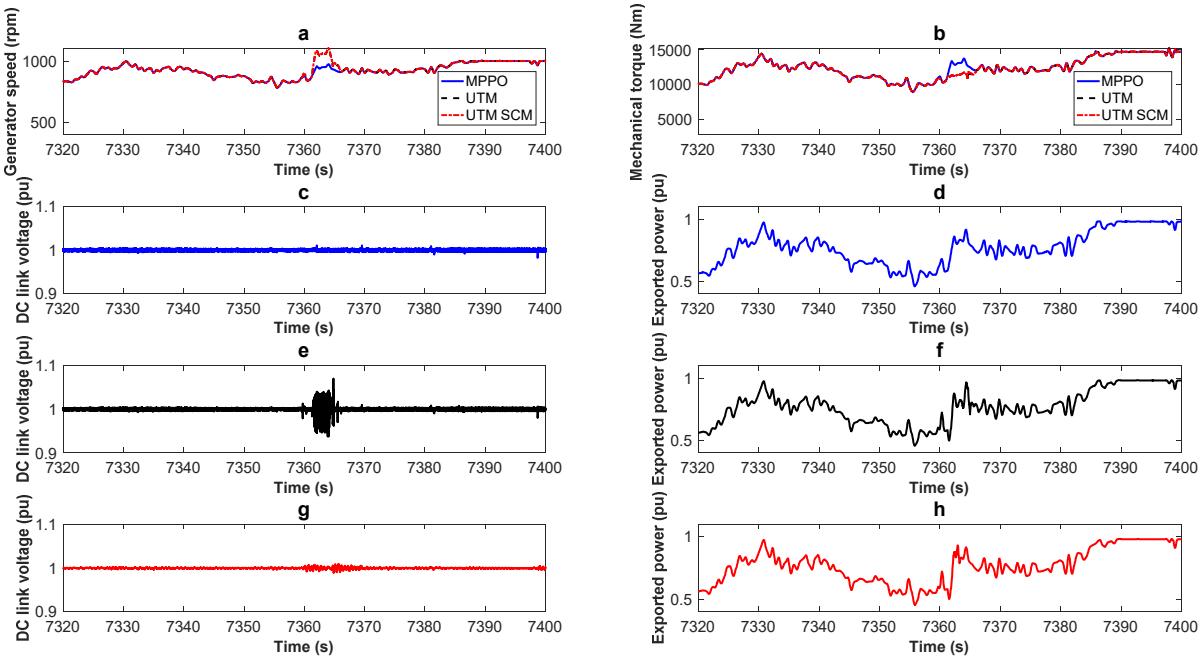


**Figure 11. Operation of the tidal system under MPPO, UTM and UTM with SCM. a. Comparison of generator speed. b. Comparison of mechanical torque input. c. DC link voltage for the MPPO case. d. Active power at the medium voltage side of the grid side transformer for the MPPO case. e. DC link voltage for the UTM case. f. Active power at the medium voltage side of the grid side transformer for the UTM case. g. DC link voltage for the UTM SCM case. h. Active power at the medium voltage side of the grid side transformer for the UTM SCM case.**

In the results presented in Figure 11, the UTM control strategy operates only between 7360s and 7370s. The rest of the time all the systems operate at MPPO. This is due to the fact that the UTM method is activated only when the *flow pulse identification signal* is on as described in Section 2.5. When the *flow pulse identification signal* is off the TCCS operates by following the maximum power point curve described in Section 2.4 and is identical to the MPPO case. Observing Figure 11b it can be seen that by activating the UTM method the sudden torque increase due to the flow pulse is effectively smoothened compared to the MPPO case. UTM and UTM SCM have similar operation regarding the reduction of the generated torque during a sudden flow pulse. In order to achieve that however a sudden increase in the generator speed is required as shown in Figure 11a.

Regarding the DC link voltage it can be seen that the voltage is kept within the limits of ±10% in all cases. When the TCCS operates at MPPO (Figure 11c) the DC link voltage appears to have some small voltage spikes at some instances due to the sudden flow changes. This means that the grid side controller described in Section 2.7 is transferring the power generated by the tidal turbine to the grid effectively. The active power exported to the grid by the TCCS for the MPPO case can also be observed in Figure 11d. The UTM case DC link voltage and active power exported to the grid are presented in Figure 11e and Figure 11f. The DC link voltage when the UTM is enabled, between 7360s and 7370s, is rippling up to ±5%. Even though this is within the allowable limits of a DC link voltage, a rippling voltage can affect the power and voltage quality at the grid side and reduce the lifetime of the electrical components at the DC link if it is occurring frequently. The grid side power for the UTM case is presented in Figure 11f and has slightly higher variation of active power compared to the MPPO case but the difference is not significant. Figure 11g presented the operation of the UTM case when the SCM is connected at the DC link and controls the voltage. It is evident that the voltage variations are minimised in the UTM SCM case compared to the UTM case. The power exported to the grid is also affected with smaller variations appearing compared to the UTM case. This is due to the fact that the SCM aim is to decrease voltage fluctuations at the DC link which does not necessarily smoothens active power.

Figure 12 shows the SCM operation for the UTM SCM case. It can be observed that the SCM is operating when the UTM is enabled between 7360s and 7370s. At these timings the contributing current which goes up to 150A at an instance provides the necessary power to keep the DC link voltage constant and the power output within acceptable limits. The state of charge of the capacitor is not affected significantly from these variations due to the fact that the SCM was sized for high power flows as discussed in Section 2.6.

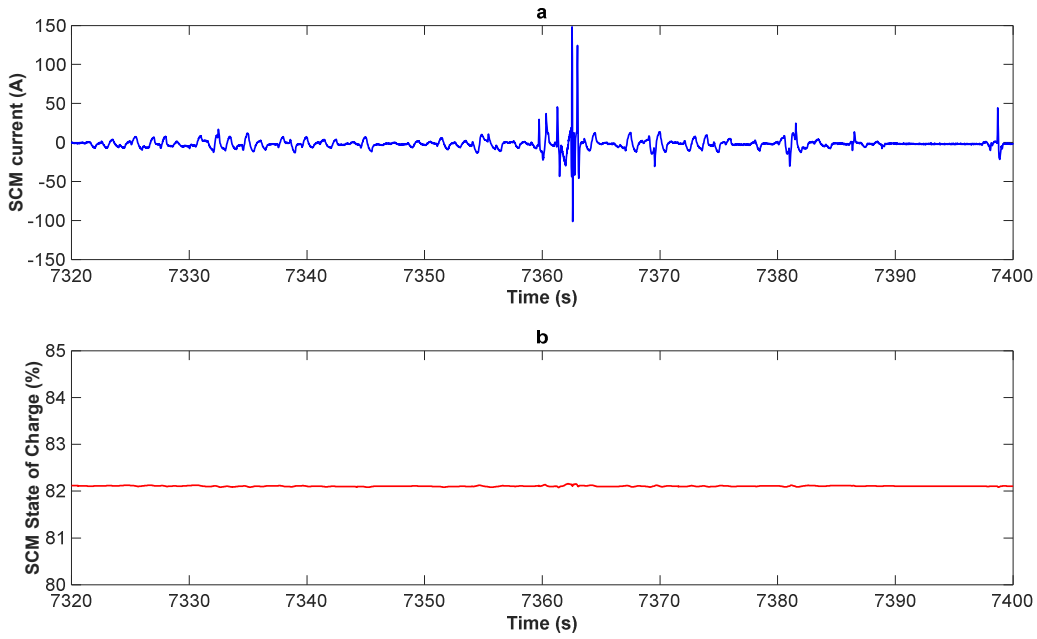


**Figure 12. SCM results for the UTM SCM case. a. SCM current contribution. b. SCM state of charge.**

Table 5 summarises results from the operation of the TCCS for the cases presented regarding averaged active power generated, averaged active power exported, voltage total harmonic distortion (VTHD) and peak voltage harmonics at the grid side.

**Table 5. Active power generated, active power exported to the grid and grid side harmonics for the three different control strategies.**

| | **MPPO** | **UTM** | **UTM SCM** |
|---|---|---|---|
| Power generated (MW) | 1.1161 | 1.1147 | 1.1149 |
| Power exported (MW) | 1.0821 | 1.0807 | 1.0809 |
| $VTHD_{max}$ (%) | 0.71 | 1.54 | 1.51 |
| $VTHD_{average}$ (%) | 0.69 | 0.71 | 0.69 |
| MoE | ±0.01 | ±0.02 | ±0.01 |

Based on the results from Table 5 it can be concluded that when using the MPPO control strategy maximum power is captured by the turbine and maximum power is injected to the grid. However, the differences compared to UTM and UTM SCM are small with the UTM SCM achieving higher power generation and injection compared to UTM. Regarding grid side harmonics, in all cases the

grid voltage harmonics are within the allowable planning limit of 4% for the case studied in this paper. The VTHD measurements from the simulation model are of very high accuracy. According to ER G5/4-1 the Class A power quality monitor has a minimum defined accuracy of 0.1%. A higher accuracy has been used in this study to comply with the recommendations. In addition, a 100s characteristic was measured and the 95$^{th}$ percentile value from the cumulative probability function was used, as recommended in ER G5/4-1, in order to calculate the Margin of Error (MoE). Since all the simulations had the same sampling points and critical value the margin of error was dependent on the standard deviation of the sample. Based on the results presented in Table 5 the standard deviation of the VTHD measurements for the UTM case was higher compared to the other two cases. Using a SCM at the DC link of the TCCS reduces $VTHD_{max}$ compared to the UTM case without SCM. The $VTHD_{max}$ appears at the point where the flow is increasing suddenly (7360s – 7365s) and the DC link voltage ripples". Reducing the grid side harmonics also has a benefit on the total losses of the TCCS. The distribution of harmonics in each case is displayed in Figure 13 at the 7360s when the UTM method is enabled. Figure 13a shows the first 100 harmonic orders where the harmonics generated by the grid side VSC are visible around the 50$^{th}$ (2500Hz) and 100$^{th}$ (5000Hz) order. Figure 13b focuses on the low order harmonics up to the 10$^{th}$ order where the largest variations between the cases are visible.

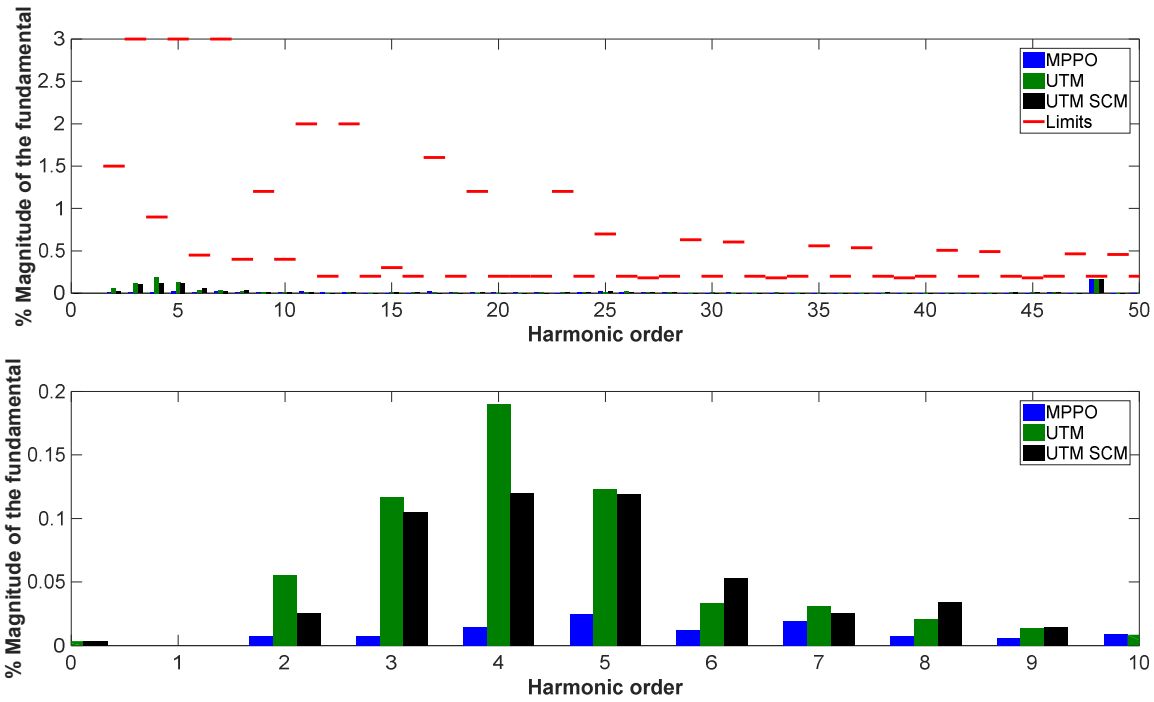


**Figure 13. Distribution of harmonics of the medium voltage grid side and the associated limits in red based on the ER G5/4-1. a. The distribution of the first 50 harmonic orders based on the engineering recommendation. b. Close view of the harmonic orders that change depending on the simulated system MPPO, UTM and UTM SCM.**

Observing Figure 13a it can stated that the system operates within limits despite sudden flow changes and changes in the way the generator side controller operates by switching from MPPO to UTM control method. A second observation from Figure 13a and the DC link voltage results of Figure 11 is that the VOC controller is operating in a desirable way, keeping the DC link voltage within limits in all cases and exports voltage within the harmonic limits. However, from Figure 13a the differences between MPPO, UTM and UTM SCM are not visible. The largest variations between the different simulated systems appear at the low order harmonics up to the $10^{th}$ order and these variations are visible in Figure 13b. It can be observed that the UTM method generates higher magnitude harmonics between the $2^{nd}$ and $5^{th}$ order compared to MPPO and UTM SCM cases. This is due to the fact that the UTM method requests larger variations of the generator speed. Voltage harmonics are transferred at multiples of the generator speed operating frequency. Comparing MPPO an UTM SCM cases it can be seen that at the low order harmonics, MPPO has minimum magnitudes whereas even with the use of the SCM the low order harmonics are quite

increased. On the other hand, it is evident that the use of a SCM can slightly decrease the increased low order harmonics generated by the UTM method.

In Section 1.2 it was stated that the most common way to reduce peak loads is to pitch the blades of the turbine. A variation of the UTM strategy can be developed so that instead of controlling the generator speed to limit the ultimate torque, the blade pitching system is used (UTM Pitch). Figure 14 compares the mechanical torque on the generator shaft for three different control strategies.

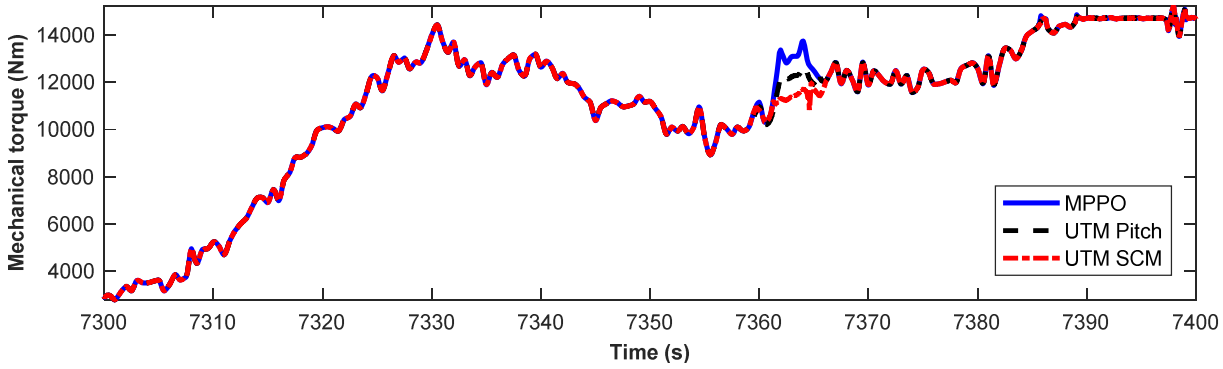


**Figure 14 Comparison of mechanical torque in the TCCS for three different control strategies, MPPO, UTM Pitch and UTM SCM.**

Observing Figure 14 it can be said that UTM Pitch can reduce the peak torque effectively though UTM SCM produces a smoother torque output. The advantage of using the UTM Pitch is the less electrical power variations created compared to the UTM methods. As it was presented in Figure 11 the UTM and UTM SCM methods generate significant electrical power variations in order to reduce the ultimate torque. These variations have an adverse effect on the DC link voltage of the TCCS and the grid side harmonics which can affect the compliance of the TCCS for grid connection. The SCM was introduced in order to minimise the adverse effects of the fluctuating electrical power. The UTM Pitch method however does not use the generator speed to control the torque but rather the pitch angle of the blades to reduce incoming torque input to the turbine from the tidal current flow. Therefore, UTM Pitch does not affect the DC link voltage or the grid side harmonics and the results are similar to those presented for the MPPO case. Reducing the torque input from the tidal current flow though has an adverse effect on total power input to the turbine. This can be seen by comparing the average power generated for the cases presented in Figure 14.

The average power generated in the MPPO case is 1.0236MW, for the UTM Pitch case 1.0185MW and for the UTM SCM case 1.0223MW. Therefore using UTM Pitch 0.5% less power is produced compared to the MPPO case. In a full tidal cycle this can be significant depending on how frequent the use of the UTM method will be.

Apart from less torque smoothing and reduced power output of the UTM Pitch method compared to the UTM SCM method, using the pitch system it is not possible to reduce torque variation but only reduce sudden torque increases. As described in Section 2.2.1 increasing the blade pitch angle reduces the hydrodynamic coefficient $C_p$ of the turbine limiting the amount of power captured from the tidal current speed. However, reducing torque variations continuously requires not only to decrease torque peaks due to sudden tidal current speed ridges but increase mechanical torque troughs when tidal current speed is decreasing. Reducing the variation of torque continuously, both peaks and troughs, can be achieved by controlling the generator speed and is presented in the next section.

## 3.2 Fatigue torque variations

The MATLAB/Simulink model of Figure 1 was simulated for 200 seconds under three cases.

- The first is the MPPO as described in Section 2.4 and presented in Section 3.1 for sudden changes in the flow speed.
- The second is the FTM control strategy described in Section 2.5 and shown in Figure 8b without a SCM at the DC link.
- The third case is the FTM control strategy with the SCM installed at the DC link.

Figure 15 shows results from the operation of the TCCS under the three cases described above.

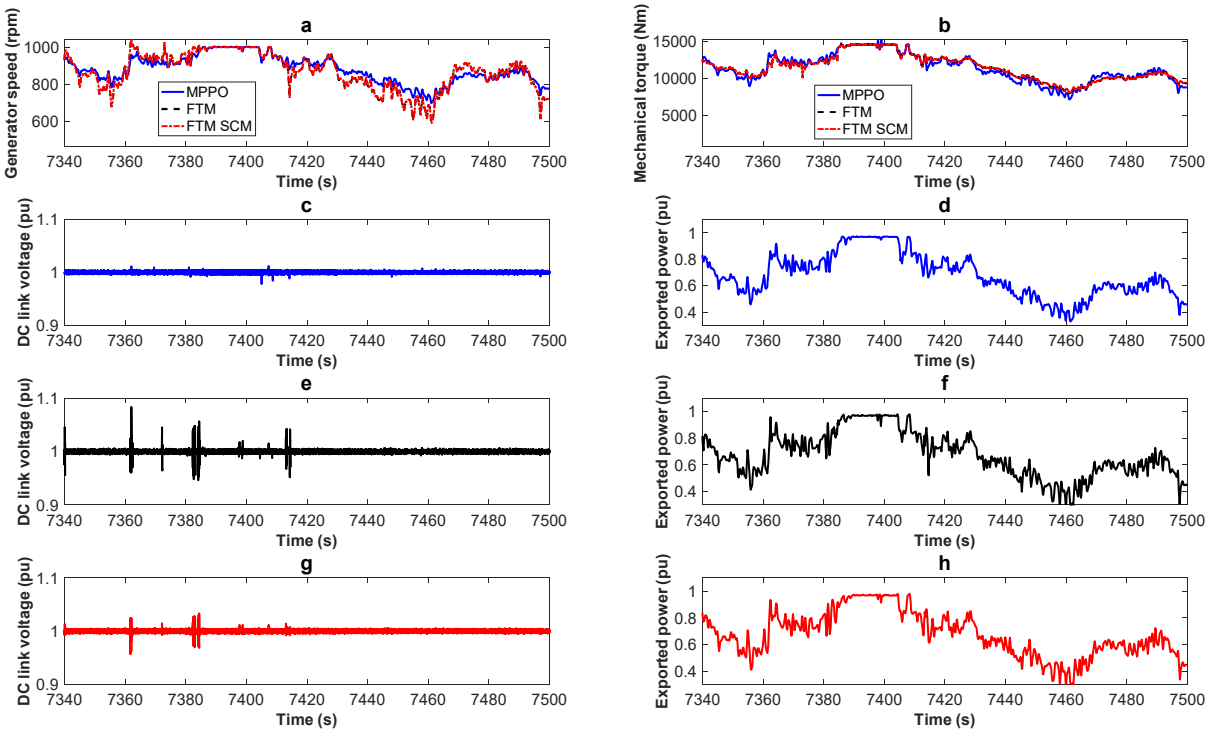


**Figure 15. Operation of the tidal system under MPPO, FTM and FTM with SCM. a. Comparison of generator speed. b. Comparison of mechanical torque input. c. DC link voltage for the MPPO case. d. Active power at the medium voltage side of the grid side transformer for the MPPO case. e. DC link voltage for the FTM case. f. Active power at the medium voltage side of the grid side transformer for the FTM case. g. DC link voltage for the FTM SCM case. h. Active power at the medium voltage side of the grid side transformer for the FTM SCM case.**

From 7300s to 7340s all three strategies operate at MPPO. At 7340s the FTM method is enabled. From 7340s the FTM and FTM SCM cases have similar generator speed and mechanical torque generated by the tidal turbine (Figure 15a and Figure 15b). The peaks and troughs from the FTM method are lower compared to the MPPO operation due to the change in the controller's aim. The mechanical torque during MPPO after 7340s averaged 11318Nm±1853Nm whereas for the FTM and FTM SCM cases the mechanical torque averaged 11408Nm±1703Nm and 11429Nm±1710Nm respectively.

Observing Figure 15e it can be seen that large voltage spikes appear at some instances when FTM is enabled. This is due to the increased fluctuations of the generator speed dictated by the FTM

method which causes higher electrical power variations. The active power exported to the grid can be compared between the MPPO and FTM methods in Figure 15d and Figure 15f respectively. The active power exported by the FTM method has slightly larger variations compared to the MPPO case. Even though the large voltage spikes of the FTM method are within the DC link voltage limits (±10%), at some instances they reach up to 9% of the DC link voltage limit in the case presented in Figure 15e. In order to ensure reliable operation these voltage spikes need to be lessened. In addition, it is beneficial for the DC link components and the power quality exported to the grid to reduce them.

This is achieved by installing the SCM at the DC link which will control the higher voltage variations. Figure 15g presents the DC link voltage of the TCCS under the FTM method but with a SCM installed at the DC link and Figure 15h the active power exported for the same case. It can be observed that the voltage spikes at the DC link are significantly mitigated. Active power exported to the grid in the FTM SCM case is similar to the FTM case since the SCM's aim is to control DC link voltage and not the smoothen the power output. However, some power spikes that appeared at around 7385s and 7415s are reduced. Apart from improving DC link voltage, connecting a SCM also affects grid compliance, power injection to the grid and power generation. Table 6 summarises these results acquired by the simulations.

**Table 6. Power generated, power injected to the grid and grid side voltage harmonics.**

| | **MPPO** | **FTM** | **FTM SCM** |
|---|---|---|---|
| Power generated (MW) | 1.0341 | 1.0304 | 1.0340 |
| Power injected (MW) | 1.0033 | 0.9996 | 0.9985 |
| $VTHD_{max}$ (%) | 0.71 | 1.75 | 1.41 |
| $VTHD_{average}$ (%) | 0.69 | 0.70 | 0.69 |
| MoE | ±0.01 | ±0.01 | ±0.01 |

The distribution of harmonics for the FTM and FTM SCM cases are similar to the ones presented in Figure 13. The FTM control strategy increases low order harmonics at multiples of the operating frequency which are reduced with the installation of the SCM. Harmonics around the switching frequency of the grid side converter are kept within the planning limits.

Figure 16 depicts the results from the operation of the SCM for the FTM SCM case. It can be seen that the contributing current from the SCM fluctuates at around 100A. This is lower compared to the 150A peak current for the UTM SCM case presented in the previous section. However, the SCM operates at more instances providing the necessary current to keep the DC link voltage constant and the electrical power output between the limits of operation. The state of charge of the SCM is not affected significantly from the fluctuating current mainly due to the sizing of the total SCM. Based on these observations and the observations in the UTM SCM case future research can focus on reducing the size and cost of such a module in order to be more attractive in a commercial scale.

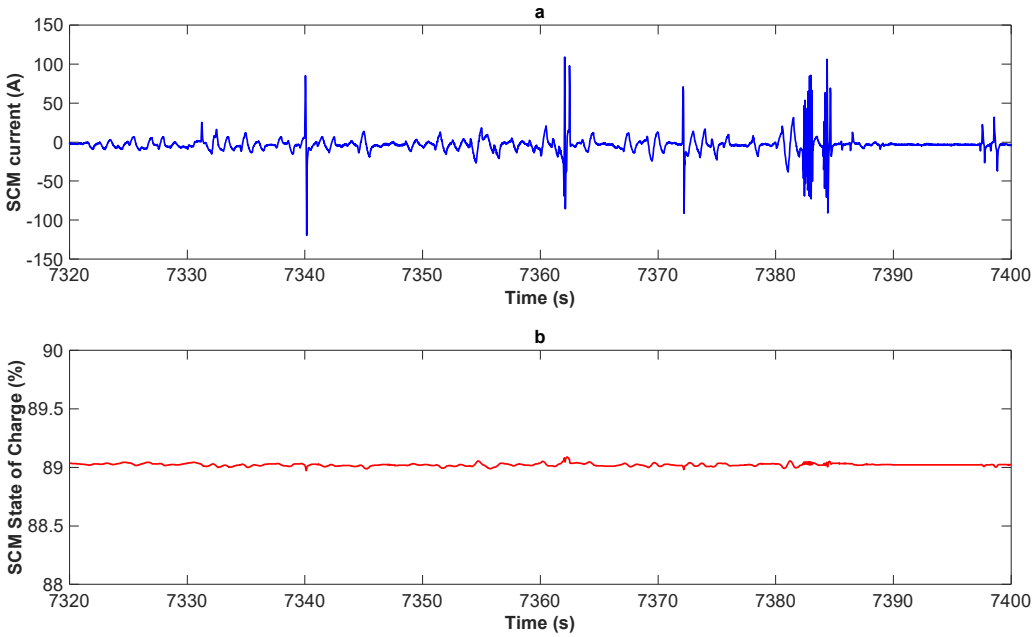


**Figure 17. SCM results for the FTM SCM case. a. SCM current contribution. b. SCM state of charge.**

## 3.3 Grid strength and tidal arrays

In sections 3.1 and 3.2 the grid is considered "strong" with 3-phase fault levels of 50MVA. With rated injected power of 1.5MW per TCCS this leads to a ratio of 33.33. In Table 7 results are presented regarding the VTHD when the TCCS using the control strategies mentioned above are connected to a weaker grid with 3-phase fault level of 30MVA.

**Table 7. Comparison of harmonics when the TCCS is connected to 50MVA and 30MVA 3-phase fault level grid.**

| 3-Phase fault (MVA) | Voltage harmonics | **MPPO** | **UTM** | **UTM SCM** | **FTM** | **FTM SCM** |
|---|---|---|---|---|---|---|
| 50 | $VTHD_{max}$ (%) | 0.71 | 1.54 | 1.51 | 1.75 | 1.41 |
| | $VTHD_{average}$ (%) | 0.69 | 0.71 | 0.69 | 0.70 | 0.69 |
| 30 | $VTHD_{max}$ (%) | 0.81 | 2.87 | 2.43 | 2.16 | 1.96 |
| | $VTHD_{average}$ (%) | 0.74 | 0.78 | 0.75 | 0.74 | 0.74 |

A small increase in the $VTHD_{average}$ can be observed when the TCCS is connected at a weaker grid. In the MPPO case this also leads a small increase of 0.1% in the $VTHD_{max}$. When a torque mitigation control strategy is used the $VTHD_{max}$ is significantly increased in a weaker grid. For the UTM case the $VTHD_{max}$ is increased from 1.54% to 2.87% and for the FTM case from 1.75% to 2.16%. The use of the SCM has a positive effect at reducing the voltage harmonic levels from 2.16% to 1.96% for the FTM case and from 2.87% to 2.43% for the UTM case. Figure 18 presents the distribution of harmonics for different cases when the 3-phase fault level is 30MVA.

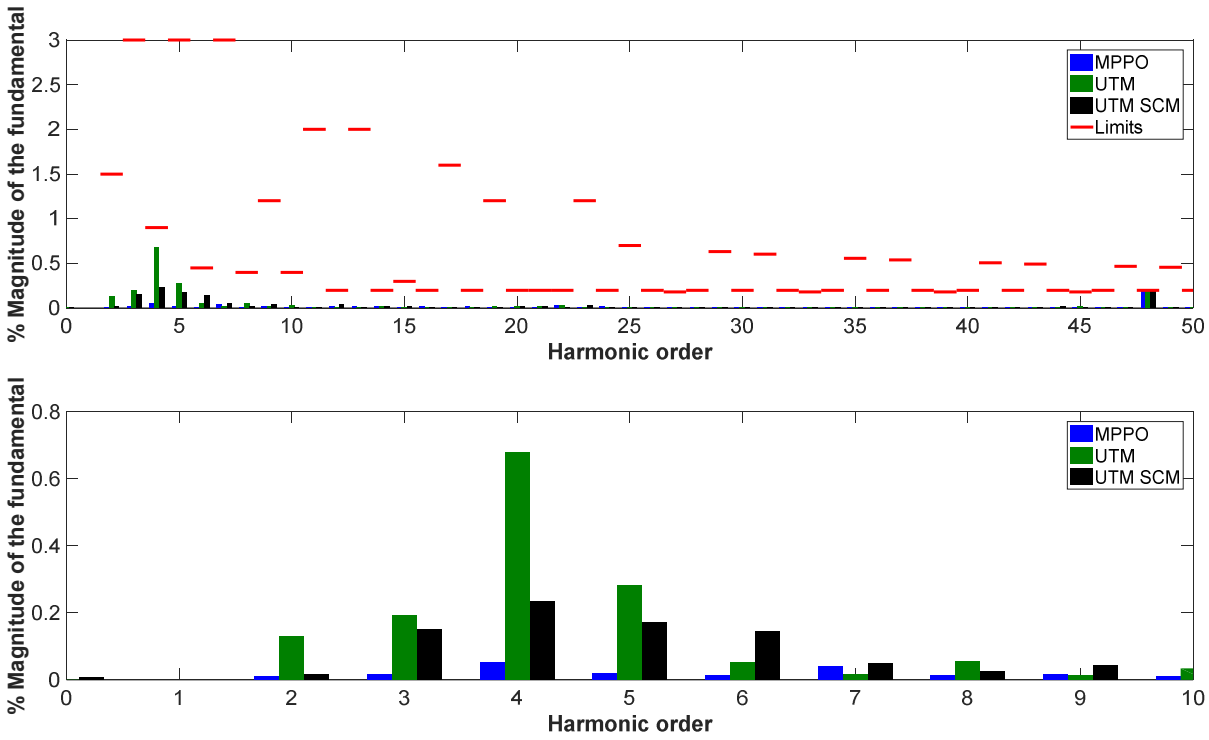


**Figure 18. Distribution of harmonics of the medium voltage grid side and the associated limits in red based on the ER G5/4-1 for 30MVA 3-phase fault levels. a. The distribution of the first 50 harmonic orders based on the engineering recommendation. b. Close view of the harmonic orders that change depending on the simulated system MPPO, UTM and UTM SCM.**

Observing the distribution of harmonics it is evident that a weaker grid is affected more by the low order harmonics generated by the torque mitigation control strategy. Figure 18a shows the first 100 harmonic orders and their limits based on the engineering recommendations. All harmonics are within the limits including the lower order harmonics and the switching frequency harmonics around the 50$^{th}$ harmonic. The addition of a SCM reduces the increased harmonic distortion generated by the UTM method to lower values. This is one of the potential uses of supercapacitors in TCCS for improving grid integration.

TCCSs will form tidal arrays in future projects. If all the TCCS in the array use the torque pulsation mitigation strategies grid compliance will be a main issue for their operation. Table 8 presents results when one, four and sixteen TCCS are connected to the same point of common coupling for 50MVA and 30MVA 3-phase fault level grid.

**Table 8 Tidal array effect on the grid side.**

| 3-Phase fault per TCCS (MVA) | Number of TCCS in the array | VTHD | MPPO | FTM | FTM SCM |
|---|---|---|---|---|---|
| 50 | 1 | $VTHD_{max}$ (%) | 0.71 | 1.75 | 1.41 |
| | | $VTHD_{average}$ (%) | 0.69 | 0.70 | 0.69 |
| | 4 | $VTHD_{max}$ (%) | 0.71 | 1.25 | 1.19 |
| | | $VTHD_{average}$ (%) | 0.68 | 0.68 | 0.68 |
| | 16 | $VTHD_{max}$ (%) | 0.71 | 1.21 | 1.11 |
| | | $VTHD_{average}$ (%) | 0.68 | 0.68 | 0.68 |
| 30 | 1 | $VTHD_{max}$ (%) | 0.81 | 2.16 | 1.96 |
| | | $VTHD_{average}$ (%) | 0.74 | 0.74 | 0.74 |
| | 4 | $VTHD_{max}$ (%) | 1.78 | 2.11 | 1.92 |
| | | $VTHD_{average}$ (%) | 0.72 | 0.73 | 0.73 |
| | 16 | $VTHD_{max}$ (%) | 0.81 | 2.02 | 1.86 |
| | | $VTHD_{average}$ (%) | 0.73 | 0.74 | 0.73 |

Based on the results presented in Table 8 two observations can be made concerning all the cases. Increasing the number of TCCS in the array does not affect $VTHD_{average}$ and slightly reduces $VTHD_{max}$. For example at 30MVA, the FTM SCM case has 1.96% $VTHD_{max}$ for one TCCS, 1.92% for four devices and 1.86% for sixteen devices. These changes are small however and only a very accurate sensor will be able to detect them. In all the cases presented in Table 8, the systems are operating within the allowable limits for all harmonic orders. This is also true for the FTM case which has the highest THD measurements compared to MPPO and FTM SCM cases. The addition of a SCM improves the compatibility of the system but it is not necessary for the integration of a TCCS with FTM control strategy to the grid.

# 4. Discussion

The research of mitigating torque pulsation can change the way TCCSs are controlled which affects active power generation. As it was shown in this paper, reducing torque pulsations can lead

to higher variability of power generated and power exported to the grid, voltage spikes at the DC link and increased harmonics of the grid side voltage. The variability of electrical power generated can be reduced by using electrical energy storage at the DC link of a TCCS. In this research paper SC are the preferred option due to the higher energy density than capacitors and higher power density than batteries. SC are particularly suited to applications that require energy pulses during short periods of time. Using commercially available SCs and a Ćuk converter a SCM is developed and modelled in order to be integrated at the DC link of the TCCS. A TCCS with a SCM can operate reliably with both UTM and FTM strategies presented in this paper. The benefits are multiple for a TCCS including reduced fatigue or peak loads due to the use of the torque pulsation mitigation strategy, improvement of power generation with the use of a SCM and reduced grid side voltage harmonics due to the SCM as well.

The variability of the generator power is also affected by tidal current speed turbulence and swell waves. In order to capture that information high resolution flow speed data, acquired from TEC mounted flow sensors during the ReDAPT project, were used as input to the turbine controller. Turbulence generates high frequency torque ripple which cannot be reduced by modifying the generator speed. There are limits imposed on the TCCS regarding the maximum acceleration and deceleration of the generator speed. As it was shown in Figure 7 a rate limiter at the speed controller ensures that the electrical torque of the generator does not change at a higher than the maximum rate. Using the FTM method the torque variations are significantly reduced with a small reduction in power generation. The reduction in power generation is minimised with the use of a SCM at the DC link of the TCCS. The torque variations due to the waves have a period of around 10 seconds which makes it possible for the controller to modify the generator speed and reduce pulsations.

Reducing torque pulsations from sudden flow speed changes or reducing the fatigue torque continuously is a choice that depends on the specific requirements of the installed TCCS. Both cases however are benefited from the use of a SCM at the DC link. As it was shown in Figure 11 the UTM method generates voltage ripples at the DC link for 6 seconds which is the total time that the UTM method is enabled. These voltage ripples are within the limits but generate harmonics at the grid side and may reduce the lifetime of components at DC link. On the other hand, the FTM

method produces sudden voltage spikes of higher value compared to the UTM method which increases the $VTHD_{max}$. The SCM can be used to eliminate voltage spikes in both cases and ensure efficient and reliable operation of the TCCS.

# 5. Conclusions

In this paper a full resource-to-wire model of a TCCS is presented. Using this model in conjunction with realistic flow inputs and a novel control strategy that aims to reduce mechanical torque pulsations, the authors investigate the potential benefits of using supercapacitors in TCCS with variable electrical power generation. Based on the results, installing a SCM with voltage mode control at the DC link of a TCCS can improve active power quality exported to the grid. The effect of a SCM at the DC link are visible when the TCCS is operated with a torque pulsation mitigation strategy. Apart from minimising voltage spikes at the DC link, a SCM can decrease voltage harmonics at the grid side and make a TCCS grid compliant even when connected to weaker grids despite the rapid active power variations. In addition, a SCM at the DC link of a TCCS can improve power generation. UTM SCM and FTM SCM cases had higher averaged power generated compared to UTM and FTM respectively. Finally, power aggregation of tidal arrays was studied and compared for TCCS that use the torque pulsation mitigation strategies and are connected to weaker grids. It is concluded that forming tidal arrays has a positive effect regarding $VTHD_{average}$ and $VTHD_{max}$.

**Acknowledgements**

Field measurements from the EMEC tidal test site were acquired under the ReDAPT project (2010-2015) which was co-funded by the Energy Technologies Institute (ETI), UK.

Funding: This work was carried out as part of the TorqTidal project, funded by EPSRC under grant EP/N035593/1.

**References**

[1] H. Ibrahim, A. Ilinca, J. Perron, Energy storage systems-Characteristics and comparisons, Renew. Sustain. Energy Rev. 12 (2008) 1221–1250. doi:10.1016/j.rser.2007.01.023.

[2] UK ENERGY IN BRIEF 2017, National Statistics, Crown copyright 2017, 2017.

[3] Black & Veatch Consulting Ltd, UK Tidal Current Resource and Economics Study, The Carbon Trust, 2011.

[4] X. Luo, J. Wang, M. Dooner, J. Clarke, Overview of current development in electrical energy storage technologies and the application potential in power system operation, Appl. Energy. 137 (2015) 511–536. doi:10.1016/j.apenergy.2014.09.081.

[5] Z. Zhou, M. Benbouzid, J. Fr?d?ric Charpentier, F. Scuiller, T. Tang, A review of energy storage technologies for marine current energy systems, Renew. Sustain. Energy Rev. 18 (2013) 390–400. doi:10.1016/j.rser.2012.10.006.

[6] Zhibin Zhou, F. Scuiller, J.F. Charpentier, M. El Hachemi Benbouzid, Tianhao Tang, Power Smoothing Control in a Grid-Connected Marine Current Turbine System for Compensating Swell Effect, IEEE Trans. Sustain. Energy. 4 (2013) 816–826. doi:10.1109/TSTE.2013.2251918.

[7] L. Sheng, Z. Zhou, J.F. Charpentier, M.E.H. Benbouzid, Stand-alone island daily power management using a tidal turbine farm and an ocean compressed air energy storage system, Renew. Energy. 103 (2017) 286–294. doi:10.1016/j.renene.2016.11.042.

[8] L. Sheng, Z. Zhou, J.F. Charpentier, M. Benbouzid, Island Power Management using a Marine Current Turbine Farm and an Ocean Compressed Air Energy Storage System, in: Proc. 11th Eur. Wave Tidal Energy Conf., 2015: pp. 1–6.

[9] Z. Zhou, F. Seuiller, J.F. Charpentier, M. Benbouzid, T. Tang, Application of flow battery in marine current turbine system for daily power management, in: 2014 First Int. Conf. Green Energy ICGE 2014, IEEE, 2014: pp. 8–13. doi:10.1109/ICGE.2014.6835389.

[10] L. Wang, J.-Y. Yu, Y.-T. Chen, Dynamic stability improvement of an integrated offshore wind and marine-current farm using a flywheel energy-storage system, IET Renew. Power Gener. 5 (2011) 387–396. doi:10.1049/iet-rpg.2010.0194.

[11] M. Minutillo, A. Lubrano Lavadera, E. Jannelli, Assessment of design and operating parameters for a small compressed air energy storage system integrated with a stand-alone renewable power plant, J. Energy Storage. 4 (2015) 135–144. doi:10.1016/j.est.2015.10.002.

[12] Z. Wang, D.S.K. Ting, R. Carriveau, W. Xiong, Z. Wang, Design and thermodynamic analysis of a multi-level underwater compressed air energy storage system, J. Energy Storage. 5 (2016) 203–211. doi:10.1016/j.est.2016.01.002.

[13] J. Mas, J.M. Rezola, Tubular design for underwater compressed air energy storage, J. Energy Storage. 8 (2016) 27–34. doi:10.1016/j.est.2016.08.006.

[14] K.P. Bassett, R. Carriveau, D.S.K. Ting, Integration of buoyancy-based energy storage with utility scale wind energy generation, J. Energy Storage. (2016). doi:10.1016/j.est.2017.04.013.

[15] R. Klar, B. Steidl, T. Sant, M. Au, R.N. Farrugia, Buoyant Energy—balancing wind power and other renewables in Europe's oceans, J. Energy Storage. (2017). doi:10.1016/J.EST.2017.07.023.

[16] L. Luznik, K.A. Flack, E.E. Lust, K. Taylor, The effect of surface waves on the performance characteristics of a model tidal turbine, Renew. Energy. 58 (2013) 108–114. doi:10.1016/j.renene.2013.02.022.

[17] I.A. Milne, R.N. Sharma, R.G.J. Flay, S. Bickerton, Characteristics of the turbulence in the flow at a tidal stream power site, Philos. Trans. R. Soc. A Math. Phys. Eng. Sci. 371 (2013) 20120196. doi:10.1098/rsta.2012.0196.

[18] I. Afgan, J. McNaughton, S. Rolfo, D.D. Apsley, T. Stallard, P. Stansby, Turbulent flow and loading on a tidal stream turbine by LES and RANS, Int. J. Heat Fluid Flow. 43 (2013) 96–108. doi:10.1016/j.ijheatfluidflow.2013.03.010.

[19] M.L. Sæterstad, Dimensioning Loads for a Tidal Turbine, Norwegian University of Science and Technology, 2011.

[20] C.R. Kennedy, S.B. Leen, C.M. Bradaigh, A preliminary design methodology for fatigue life prediction of polymer composites for tidal turbine blades, Proc. Inst. Mech. Eng. Part L J. Mater. Des. Appl. 226 (2012) 203–218. doi:10.1177/1464420712443330.

[21] B. Whitby, C.E. Ugalde-Loo, Performance of Pitch and Stall Regulated Tidal Stream Turbines, IEEE Trans. Sustain. Energy. 5 (2014) 64–72. doi:10.1109/TSTE.2013.2272653.

[22] M.R. Motley, R.B. Barber, Passive control of marine hydrokinetic turbine blades, Compos. Struct. 110 (2014) 133–139. doi:10.1016/j.compstruct.2013.11.026.

[23] K. Gracie-Orr, T.M. Nevalainen, C.M. Johnstone, R.E. Murray, D.A. Doman, M.J. Pegg, Development and initial application of a blade design methodology for overspeed power-

regulated tidal turbines, Int. J. Mar. Energy. 15 (2016) 140–155. doi:10.1016/j.ijome.2016.04.006.

[24] M.C. Sousounis, J.K.H. Shek, Mitigation of Torque Pulsations in Variable Pitch Tidal Current Turbines Using Speed Control, in: Proc. 12th Eur. Wave Tidal Energy Conf., Cork, Ireland, 2017: pp. 1146-1–9.

[25] UKERC Energy Data Centre, (2015) 2017. http://ukerc.rl.ac.uk/ (accessed December 30, 2017).

[26] Met-Ocean Data Science for Offshore Renewable Energy Applications, (2017). http://redapt.eng.ed.ac.uk/index.php (accessed March 19, 2018).

[27] J. McNaughton, S. Harper, R. Sinclair, B. Sellar, Measuring and modelling the power curve of a Commercial-Scale tidal turbine, in: Proc. 11th Eur. Wave Tidal Energy Conf., Nantes, 2015: pp. 1–9.

[28] D.R.J. Sutherland, B.G. Sellar, S.F. Harding, I. Bryden, Initial flow characterisation utilising turbine and seabed installed acoustic sensor arrays, in: Proc. 10th Eur. Wave Tidal Energy Conf. Ser., Aalborg, Denmark, 2013.

[29] B.G. Sellar, D.R.J. Sutherland, D.M. Ingram, V. Venugopal, Measuring waves and currents at the European marine energy centre tidal energy test site: Campaign specification, measurement methodologies and data exploitation, in: Ocean. 2017 - Aberdeen, IEEE, 2017: pp. 1–7. doi:10.1109/OCEANSE.2017.8085001.

[30] NWTC Information Portal (HARP_Opt), (2016) 2017. https://nwtc.nrel.gov/HARP_Opt (accessed March 19, 2018).

[31] S. Heier, Wind Energy Conversion Systems, in: Grid Integr. Wind Energy Onshore Offshore Convers. Syst., 3rd ed., John Wiley & Sons, Ltd., 2014: pp. 31–117.

[32] M.C. Sousounis, J.K.H. Shek, R.C. Crozier, M.A. Mueller, Comparison of Permanent Magnet Synchronous and Induction Generator for a Tidal Current Conversion System with Onshore Converters, in: Ind. Technol. (ICIT), 2015 IEEE Int. Conf., IEEE, 2015: pp. 2481–2486. doi:10.1109/ICIT.2015.7125463.

[33] Energy Networks Association, Planning Levels for Harmonic Voltage Distortion and the Connection of Non- Linear Equipment to Transmission Systems and Distribution Networks in the United Kingdom, 2005.

[34] A. Ioinovici, Power Electronics and Energy Conversion Systems: Fundamentals and Hard-

switching Converters, Volume 1, John Wiley & Sons, Ltd, Chichester, UK, 2013. doi:10.1002/9781118443040.

[35] M.C. Sousounis, L.K. Gan, A.E. Kiprakis, J.K.H. Shek, Direct drive wave energy array with offshore energy storage supplying off-grid residential load, IET Renew. Power Gener. 11 (2017) 1081–1088. doi:10.1049/iet-rpg.2016.0032.

[36] MAXWELL TECHNOLOGIES, (2016) 2016. http://www.maxwell.com/ (accessed November 27, 2017).

[37] M. Zarif, M. Monfared, Step-by-step design and tuning of VOC control loops for grid connected rectifiers, Int. J. Electr. Power Energy Syst. 64 (2015) 708–713. doi:10.1016/j.ijepes.2014.07.078.